Published in final edited form as:
*Neuroimage*. 2009 March ; 45(1 Suppl): S99–110. doi:10.1016/j.neuroimage.2008.10.051.

# Continuous Medial Representation of Brain Structures Using the Biharmonic PDE

**Paul A. Yushkevich**[a,*]

a *Penn Image Computing and Science Laboratory (PICSL), Department of Radiology, University of Pennsylvania, Philadelphia, PA, USA*

## Abstract

A new approach for constructing deformable continuous medial models for anatomical structures is presented. Medial models describe geometrical objects by first specifying the skeleton of the object and then deriving the boundary surface corresponding to the skeleton. However, an arbitrary specification of a skeleton will not be "Valid" unless a certain set of sufficient conditions is satisfied. The most challenging of these is the non-linear equality constraint that must hold along the boundaries of the manifolds forming the skeleton. The main contribution of this paper is to leverage the biharmonic partial differential equation as a mapping from a codimension-0 subset of Euclidean space to the space of skeletons that satisfy the equality constraint. The PDE supports robust numerical solution on freeform triangular meshes, providing additional flexibility for shape modeling. The approach is evaluated by generating continuous medial models for a large dataset of hippocampus shapes. Generalizations to modeling more complex shapes and to representing branching skeletons are demonstrated.

### Keywords

Medial Representation; Skeletons; Deformable Models; Computational Anatomy; Shape Analysis

## 1. Introduction

*Medial representations* (m-reps) (Pizer et al., 2003a; Joshi et al., 2002) and the more recent *continuous medial representations* (cm-reps) (Yushkevich et al., 2006; Terriberry and Gerig, 2006) are deformable geometric models that describe anatomical structures by explicitly defining the topology and shape of a structure's skeleton and then deriving the geometry of the structure's boundary from the skeleton. Models are subsequently deformed to fit target data by modifying the parameters defining the skeleton. Deformable medial modeling has been used in a variety of medical imaging analysis applications, including computational neuroanatomy (Styner et al., 2004, 2003b; Yushkevich et al., 2007, 2008), cardiac modeling (Sun et al., 2008a), and cancer treatment planning (Stough et al., 2007; Crouch et al., 2007; Pizer et al., 2005). The primary appeal of medial modeling is that it enables *shape features derived from skeletons* to be used in statistical analysis, e.g., for comparing the shape of anatomical structures between cohorts. Principal among these features is *thickness*, defined here as the distance

*Corresponding author. Address: 3600 Market St., Ste 370, Philadelphia, PA 19104, USA, Email address: E-mail: pauly2@mail.med.upenn.edu (Paul A. Yushkevich).

between the skeleton and and boundary, a feature of great importance in neuromorphometry. Other features, such as the curvature of the skeleton, can also be highly descriptive of the local shape properties of an object. Another attractive feature of deformable medial modeling is the ability to define a natural shape-based coordinate system over the interiors of structures, which leads to natural applications in structure-specific normalization and statistical mapping (Yushkevich et al., 2007, 2008).

Medial modeling should be distinguished from *skeletonization* (Kimia et al., 1995; Ogniewicz and Kübler, 1995; Näf et al., 1996; Golland et al., 1999; Siddiqi et al., 1999b,a; Thompson et al., 2003; Bouix et al., 2005), an approach where the skeleton is derived from the boundary representation deterministically. The difference between skeletonization and medial modeling is summarized in Fig. 1. Skeletonization has limited utility in morphometric analysis studies because the number and configuration of the branches in the skeleton (commonly referred to as *branching topology*) is highly sensitive to boundary noise. In the case of anatomical structures, branching topology is likely to vary between subjects, requiring the skeleton to be simplified (or pruned) prior to performing shape analysis. By contrast, deformable modeling can assure that the topology of the skeleton representation remains the same for all subjects in the study. The drawback of this approach is that the deformable medial models can only offer an approximate representation of the underlying anatomical structures. However, in practice the representation error is small in comparison to the errors associated with the segmentation of anatomical structures in medical images (Styner et al., 2003a; Yushkevich et al., 2006).

The premise of continuous medial modeling is that the specification of the skeleton must be given as a continuous manifold (or a set of manifolds) — or as a discrete mesh that can be successively refined towards a continuous limit. The boundary derived from the skeleton by inverse skeletonization should also be a continuous surface (or refinable towards a continuous limit). Most importantly, the “actual” skeleton of this boundary surface should be the same as the “synthetic” skeleton specified by the model. This last requirement leads to a set of non-linear equality constraints than the synthetic skeleton must satisfy along curves that bound its component manifolds, as well as a set of inequality constraints that the skeleton must satisfy at every point (Damon, 2003, 2004). In deformable modeling applications these constraints lead to severely over-constrained optimization problems because the number of points where they must be satisfied is infinite (or at least, very large), while the number of coefficients (or control points) defining the skeleton is finite and, preferably, small.

A number of solutions to addressing this challenge have been proposed. In (Yushkevich et al., 2003), the authors adapted the shape of the domain on which the skeleton is defined so as to force the equality constraints to hold along its boundary. This method is limited to single-manifold skeletons and also presents difficulties for establishing correspondences between models fitted to different instances of a structure. In (Yushkevich et al., 2006), skeletons were defined as solutions of a Poisson partial differential equation (PDE) with a *non-linear* boundary condition that incorporates the equality constraint. The advantage of the PDE is that it provides a bijective mapping from a subset of a vector space to the space of synthetic skeletons satisfying the equality constraint, allowing linear statistical analysis; but the approach has its limitations: solving the non-linear Poisson equation is computationally expensive and the idea does not extend to skeletons with multiple branches. More recently, Terriberry and Gerig (2006) used a specially modified subdivision surface scheme to force local geometry near the edges of skeletal manifolds to satisfy the equality constraint. The technique can handle medial branching. One limitation of this approach is that it requires skeletons to be defined using meshes with quadrilateral elements. By contrast, the method proposed in this work is independent of the type of approach used to model skeleton manifolds. The underlying surface representation can be based on harmonic basis functions, splines or subdivision surfaces with triangular elements.

The main contribution of this work is to use the biharmonic PDE $\Delta^2 u = f$ to create a high-dimensional mapping from a *parameter space* that is a codimension-0 subset of Euclidean space to the space of synthetic skeletons satisfying the required equality constraints. Unlike the Poisson PDE used for this purpose in (Yushkevich et al., 2006), the higher-order biharmonic equation can incorporate the equality constraints as *linear* boundary conditions, leading to a simpler, more robust numerical problem. Furthermore, the mapping defined through the biharmonic equation is not limited to single-manifold skeletons.

The paper is organized as follows. The necessary background on medial geometry and inverse skeletonization is given in Sec. 2. The new approach based on the biharmonic equation is presented in Sec. 3. Sec. 4 presents an evaluation of the method in a large hippocampus dataset and shows examples of cm-rep models fitted to other brain structures. Sec. 5 includes discussion and examples of the generalization of the PDE-based model to branching skeletons.

## 2. Background

This section summarizes some of the main properties of skeletons. Facts from medial geometry are given without proof, and we refer the reader to Damon's extensive work for a more mathematical treatment of the subject (Damon, 2003, 2004, 2005).

### 2.1. Blum Skeleton Definition

In what follows, we use Blum's definition of the skeleton (Blum, 1967), which was originally given in two dimensions but has a three-dimensional equivalent that has been studied extensively in the recent literature (Nackman, 1982; Vermeer, 1994; Giblin and Kimia, 2003, 2004; Pizer et al., 2003b; Damon, 2003, 2004, 2005).

There are several ways to define the Blum skeleton of an object: as the crest of the distance transform from the boundary; as the shock set of the Eikonal PDE; or, as we do below, as the locus formed by the maximal inscribed balls.

**Definition 1—**A closed bounded set $o \subset \mathbb{R}^3$ is called a geometric object if it is homeomorphic to a ball in $\mathbb{R}^3$ and if its boundary, denoted $\partial o$, is a smooth generic surface. Following (Giblin and Kimia, 2003), the term generic means devoid of singularities that can be removed by applying a small perturbation to the surface.

**Definition 2—**A ball $b$ is called a maximal inscribed ball (MIB) in a geometric object $o$ if $b \subset o$ and there exists no ball $b' \neq b$ such that $b \subset b' \subset o$.

**Definition 3—**The skeleton of a geometric object $o$ is the locus of points in $\mathbb{R}^3 \times \mathbb{R}^+$ formed by the centers and radii of all MIBs in $o$.

The locus formed by the centers of the MIBs in $\mathbb{R}^3$ is a *Whitney stratified set* (Damon, 2005), *i.e.* a set formed by one or more *manifolds with boundary* connected along their boundaries. We will refer to these manifolds as *medial manifolds.* We will use the term *medial seam* to refer to portions of medial manifold boundaries that are shared by multiple medial manifolds, and use the term *medial edge* to refer to the remaining, non-shared portions of medial manifold boundaries. We will use the term *radial scalar field* to refer to the field formed by the radii of the MIBs along the medial manifolds. A simple example of a branching skeleton is shown in Fig. 2.

Giblin and Kimia (2004) prove that points that generically occur on skeletons of geometric objects fall into five distinct classes, which are characterized by the order and multiplicity of contact between the MIB and the object's boundary: (1) points on the interior of medial

manifolds, where the MIB is tangent to the object's boundary at two points; (2) points on medial edges, where the MIB is tangent to the boundary at one point and has third-order contact with the boundary; (3) points on medial seams, where the MIB is tangent to the boundary at three points; (4) points at seam-edge intersections; and (5) points at seam-seam intersections. Giblin and Kimia (2004) also point out that the geometry of points at edges and seams of medial manifolds is the limit case of the geometry of points on the interior of medial manifolds. For example, one walks along the medial manifold towards a point on the medial edge, the points of tangency between the object's boundary and the MIB centered at one's location will get closer and closer to each other, collapsing to a single point once the medial edge is reached.

### 2.2. Skeleton-Boundary Relationship

The analytic relationship between the skeleton $\mathcal{S}$ of an object and its boundary $\mathcal{B}$ can be established on the basis of the mapping between the centers of MIBs and the points of tangency between the MIBs and $\mathcal{B}$ Every point on $\mathcal{B}$ is associated with a single point on $\mathcal{S}$, since there can only be one MIB tangent to $\mathcal{B}$ at a given point. Conversely, every point on $\mathcal{S}$ is associated with one, two or three points on $\mathcal{B}$, depending whether it lies on the medial edge, medial interior or medial seam. The bitangency is the generic case, and the other cases are limit cases of the bitangent MIB geometry.

Let $\mathbf{b}^+$ and $\mathbf{b}^-$ denote the points of tangency between $\mathcal{B}$ and a bitangent MIB with center $\mathbf{m}$ and radius $R$. It can be shown (e.g., (Damon, 2004)) that $\mathbf{b}^\pm$ can be expressed analytically in terms of $\mathbf{m}$ and $R$, as follows:

$$\mathbf{b}^\pm = \mathbf{m} + R\mathbf{U}^\pm, \tag{1}$$

where $\mathbf{U}^\pm$ are the unit outward normal vectors to $\mathcal{B}$ at the points $\mathbf{b}^\pm$. These normals are given in turn by

$$\mathbf{U}^\pm = -\nabla_{\mathbf{m}} R \pm \sqrt{1 - |\nabla_{\mathbf{m}} R|^2}\,\mathbf{N}_{\mathbf{m}}, \tag{2}$$

where $\mathbf{N}_{\mathrm{m}}$ is the unit normal of the medial manifold at $\mathbf{m}$ and $\nabla_{\mathrm{m}} R$ is the Riemannian gradient of $R$ on the medial manifold (Fig 3 gives an illustration of this geometry in 2D). Recall that the centers of bitangent MIBs lie on the interior of medial manifolds in $\mathcal{S}$ (i.e., not on the edges or seams); thus $\mathbf{m}$ and $R$ are continuous and differentiate in the neighborhood of a bitangent MIB.

Let us now consider the limit behavior of (2) as we approach the edges and seams of medial manifolds. As noted above, the MIBs centered along medial edges are tangent to $\mathcal{B}$ at a single point. For $\mathcal{B}$ to be continuous, this requires $\mathbf{b}^-$ and $\mathbf{b}^+$ to collapse to a single point as the medial edge is approached. That, in turn, requires the coefficient of $\mathbf{N}_{\mathrm{m}}$ in (2) to be 0, leading to the following condition:

$$|\nabla_{\mathbf{m}} R| = 1 \ \text{along medial edges}. \tag{3}$$

A similar situation occurs at medial seams. The seam is shared by three medial manifolds, so as we approach a point m on a medial seam, we have $\mathbf{m}_1 \to \mathbf{m}$, $\mathbf{m}_2 \to \mathbf{m}$, and $\mathbf{m}_3 \to \mathbf{m}$. For the boundary to be continuous, the six MIB tangency points $\mathbf{b}_1^\pm, \mathbf{b}_2^\pm, \mathbf{b}_3^\pm$ must collapse to three points: $\mathbf{b}_1^+ \to \mathbf{b}_2^-, \mathbf{b}_2^+ \to \mathbf{b}_3^-$ and $\mathbf{b}_3^+ \to \mathbf{b}_1^-$. This requirement can again be expressed in terms of the gradient of $R$, as follows:

$$\nabla_{\mathbf{m}_{i\oplus 1}} R - \nabla_{\mathbf{m}_{i\ominus 1}} R = \sqrt{1 - |\nabla_{\mathbf{m}_i} R|}\,\mathbf{N}_{\mathbf{m}_i} \quad (4)$$

where $i = 1,2,3$ and $\oplus$, $\ominus$ denote addition and subtraction modulo 3.

In addition to the three cases examined above, there are two special situations at seam-edge and seam-seam intersections that can be treated as limit cases of corresponding conditions. However, we do not deal with these situations in the current paper.

### 2.3. Inverse Skeletonization

In deformable medial modeling, models for anatomical structures are formed as follows: first, a *synthetic skeleton* is defined as a manifold (or, in the branching case, a collection of manifolds) with a scalar radius field; second, the boundary of the structure is derived from the synthetic skeleton using relations (1) and (2); lastly, the parameters defining the synthetic skeleton are modified to maximize the match between the model and the structure of interest (as Fig. 1 illustrates). Central to this scheme is the problem of *inverse skeletonization:* under which conditions does a synthetic skeleton $\mathcal{S}_{\text{syn}}$ happen to be the geometrical skeleton of some object *o*? It is easy to devise examples where inverse skeletonization fails, i.e., of synthetic skeletons for which (1) and (2) give discontinuous or self-intersecting boundary surfaces (see Fig. 4 in (Yushkevich et al., 2006)).

For single-manifold synthetic skeletons, the sufficient conditions for inverse skeletonization are given in (Yushkevich et al., 2006, Theorem 1). These conditions consist of the nonlinear equality relation (3) and several inequality constraints. From the point of view of continuous modeling, the equality constraint presents a much greater challenge than the inequality constraints. If the medial manifold in $\mathcal{S}_{\text{syn}}$ is defined using a finite set of continuous basis functions, there are as many degrees of freedom as there are basis functions, while there are infinitely many points at which the equality constraint (3) must be satisfied. This leads to a severely over determined system, which is the main challenge of continuous medial modeling. For skeletons with multiple medial manifolds the situation is similar, with (4) becoming an equality constraint that must be satisfied along medial seams.

## 3. Methods

### 3.1. Fundamental Problem of Continuous Medial Modeling

Continuous medial modeling relies on our ability to generate valid synthetic skeletons (those satisfying the necessary equality and inequality constraints) and to perform gradient descent optimization in the space of valid synthetic skeletons. More formally, we pose the fundamental problem of continuous medial modeling in the following form: *find a continuous differentiable mapping from a co-dimension zero subset of* $\mathbb{R}^N$ onto the space of all synthetic skeletons satisfying equality constraints (3) and (4).

This is a very general statement of the problem. It turns out it is sufficient to restrict our attention to the radial part of the mapping, while allowing the mapping to preserve the medial manifolds. Thus, in the single-manifold case, the problem becomes the following: given a medial manifold $\mathbf{m} \in \mathbb{R}^3$, find a mapping from a co-dimension zero subset of $\mathbb{R}^N$ onto the set of all radial fields $R$ defined over $\mathbf{m}$ that satisfy (3). As we show below, this problem has a solution. Furthermore, the solution can generalize to branching skeletons, as we demonstrate in Sec. 5.3.

### 3.2. Medial Modeling via the Biharmonic PDE

Let $\partial\mathbf{m}$ denote the boundary of $\mathbf{m}$ and let $\gamma(s)$: $[0, L) \rightarrow \mathbb{R}^3$ be its parametric form, parameterized by the arclength $s$, where $L$ is the length of $\partial\mathbf{m}$. Let $\boldsymbol{T}_\gamma(s)$ be the unit tangent vector along $\gamma$ and let $\boldsymbol{\nu}(s)$ be the outward unit normal vector along $\gamma$ $(s)$, i.e., $\boldsymbol{\nu} \perp \mathbf{N}_\mathbf{m}$ and $\boldsymbol{\nu} \perp \boldsymbol{T}_\gamma$. Note that

$$\nabla_\mathbf{m} R = R_{,s}\, T_\gamma + R_{,\nu}\, \nu,$$

where $R_{,s}$ and $R_{,\boldsymbol{\nu}}$ denote the partial derivative of $R$ with respect to $s$ and $\boldsymbol{\nu}$, respectively. This expression allows us to rewrite the equality constraint (3) as

$$R_{,\nu}|_\gamma = -\sqrt{1 - (R_{,s})^2}, \tag{5}$$

where the sign is negative because $R$ increases in the inward direction from the medial edge. The central idea of this paper is the observation that if we were to be given the value of $R$ along the edge $\gamma$, i.e.,

$$R|_\gamma = \tau(s) \tag{6}$$

then, together, the specification (6) and the constraint (5) have precisely the form of the *Dirichlet boundary condition for a fourth-order PDE.* This fact allows us to define $R$ on the interior of the medial manifold $\mathbf{m}$ as a solution of the fourth-order biharmonic PDE.

It turns out more convenient to define such a PDE not in terms of $R$ itself, but in terms of another function, $\varphi = R^2$. Let $\rho \in L^2(\mathbf{m})$ be a two-dimensional scalar field on $\mathbf{m}$ and let $\tau \in L^2(\partial\mathbf{m})$ be a one-dimensional scalar field on $\gamma$, such that $\tau > 0$ and $|\mathrm{d}\tau/\mathrm{d}s| < 1$ everywhere on $\gamma$. Then let $\varphi$ satisfy

$$\begin{aligned} &\Delta^2_\mathbf{m}\varphi = \rho, \\ &\varphi|_\gamma = \tau^2, \\ &\varphi_{,\nu}|_\gamma = -2\tau\sqrt{1 - (\mathrm{d}\tau/\mathrm{d}s)^2}, \end{aligned} \tag{7}$$

where $\Delta_\mathbf{m}$ denotes the Laplace-Beltrami operator (LBO) on the manifold $\mathbf{m}$.

Note that the boundary conditions in this equation are simply the result of substituting $R = \sqrt{\varphi}$ into (6) and (5), respectively, and carrying out the chain rule. Provided that the solution $\varphi$ is non-negative everywhere on $\mathbf{m}$, it is easy to verify that $R = \sqrt{\varphi}$ satisfies the equality constraint (3) on $\partial\mathbf{m}$.[1] Ensuring that $\varphi > 0$ is non-trivial: while the maximum principle for the

[1]Indeed, taking the square of the second boundary condition in (7), substituting $\sqrt{\varphi}$ for $\tau$ and noting that

$$|\nabla_\mathbf{m}\varphi|^2 = (\varphi_{,\nu})^2 + (\varphi_{,s})^2 \text{ on } \partial\mathbf{m},$$

we get $|\nabla_\mathrm{m}\varphi|^2 = 4\varphi$ and, by the chain rule, $|\nabla_\mathrm{m}R|^2 = 1$.

biharmonic operator can give us a sufficient condition, this condition is too restrictive to use in practice because it excludes a wide range of positive solutions. In practice, however, there is no difficulty staying in the range of positive solutions in the course of deformable modeling.

The PDE (7) is a linear operator

$$\varphi=\Psi(\rho,\tau),\ \text{where}\ \Psi:L^2(\mathbf{m})\times L^2(\gamma)\rightarrow L^2(\mathbf{m}).$$

The existence, uniqueness and stability of the first biharmonic equation (Glowinski and Pironneau, 1979) ensure that the mapping $\varphi = \Psi(\rho,\tau)$ is defined everywhere on its domain, is one-to-one, and is differentiable. Conveniently, the operator $\Psi$ maps zeros to zero, i.e., if $\rho = 0$ everywhere on $\mathbf{m}$ and $\tau(s) = 0$ everywhere on $\gamma$, then $\varphi_{,\mathbf{v}}$ vanishes on $\partial\mathbf{m}$ and $\varphi = 0$ is the solution of the PDE (7). Interestingly, we define the PDE in terms of $\varphi = R$ rather than $\varphi = R^2$, we would lose this attractive property. Another attractive reason for choosing $\varphi = R^2$ is that for an ellipsoid, the simplest 3D object with a single-manifold medial axis, $\Delta\varphi$ is constant on $\Omega$ and $\Delta^2\varphi = 0$. This is not the case for $\varphi = R$.

### 3.3. Numerical Solution

Implementing medial modeling based on the biharmonic PDE involves choosing an appropriate representation for the manifolds composing the medial model and then defining a finite differences scheme that allows us to solve the PDE numerically as a sparse linear system.

**3.3.1. Numerical Representation of Medial Models—**Our choice of representation for the medial manifolds is *Loop subdivision surfaces* (Loop, 1987). This representation is simple, can be defined on an arbitrary domain and, with a small modification, can be used to represent multi-manifold medial models. In the Loop scheme, a coarse-level triangular mesh is successively subdivided, converging to a continuous limit surface. Subdivision involves splitting triangles into four by inserting a new vertex in every edge. The coordinates of the new vertices, as well as the coordinates of the vertices retained from the previous level, are computed at each iteration using simple arithmetic rules (Loop, 1987). Edges in the mesh can be designated as *crease edges*, and special rules are used at these edges to generate a crease in the limit surface (Biermann et al., 2000).

In deformable modeling, the model must be defined by a set of coefficients which can be modified in order to deform the model (Fig 1). In our Loop-based scheme, the coefficients are used to specify the coarse-most mesh $(\mathcal{V}^0,\mathcal{T}^0)$, where $\mathcal{V}$ denotes the vertices and $\mathcal{T}$ are the triangles. Each vertex $i$ is a tuple of coefficients: $\mathcal{V}^0=(\mathbf{m}_i^0,\rho_i^0,\tau_i^0)$, where $\mathbf{m}_i^0 \in \mathbb{R}^3$, and $\rho_i^0$ and $\tau_i^0$ are scalars, corresponding to the boundary conditions of (7). Although we are only interested in the values of $\tau$ along $\gamma$ $(s)$, i.e., at the edges of the medial manifolds, it is more convenient to define $\tau_i^0$ at each vertex and to ignore its values an non-edge vertices. [2]

While the mesh $(\mathcal{V}^0,\mathcal{T}^0)$ serves as the specification of the deformable model's coefficients, the model itself, in theory, is given by the limit surface of Loop subdivision. In practice, however, we approximate this limit surface by applying a finite number of subdivisions, i.e., using the mesh $(\mathcal{V}^k, \mathcal{T}^k)$ as a digital representation of the skeleton $\mathbf{m}$ and scalar field $\rho$ and $\tau$. The level of subdivision $k$ is chosen empirically. During model fitting, $k$ is usually between

[2]In the Loop subdivision scheme, the vertices computed along the edges of a child-level surface only depend on the edge vertices in the parent-level surface, so having dummy $\tau$-values denned at non-edge vertices has no effect on the PDE solution.

1 and 3, depending on the density of $(\mathcal{V}^0,\mathcal{T}^0)$. Once the model has been fitted to the target object, $k$ may be increased to generate a high-quality model.

**3.3.2. Spectral Deformation for Medial Manifolds—**In practice, when fitting models to anatomical data, we do not always want to optimize directly over the vertices of the coarse-level mesh $(\mathcal{V}^0,\mathcal{T}^0)$. In our experiments, the control mesh will typically have around 100 vertices, which is too many parameters to optimize in the early stages of model fitting. Instead, we leverage spectral decomposition of the control mesh to allow greater *global control*, leading to a more efficient coarse-to-fine strategy.

Spectral decomposition involves defining an orthogonal basis on the control mesh $(\mathcal{V}^0,\mathcal{T}^0)$, so that the mesh can be deformed smoothly by modifying the coefficients of a small number of basis functions rather than the vertices of the control mesh. The natural approach to defining an orthogonal basis on an arbitrary 3D mesh is to use the *eigenfunctions of the Laplace operator*, which is the generalization of the Fourier basis on the plane (as well as the the spherical harmonics basis on the sphere). The Laplace eigenfunction basis has become a popular tool for mesh compression and deformable modeling (Karni and Gotsman, 2000; Rustamov, 2007), and has found applications in computational neuroanatomy (Thompson et al., 2004; Chung et al., 2005; Qiu et al., 2006).

Our implementation of the Laplace eigenfunction basis follows the approach prescribed in (Belkin and Niyogi, 2003), using a variant the authors call “simple-minded”, where the Laplace operator is defined based on mesh topology rather than using mesh coordinates. Specifically, the Laplace operator for a function $\psi$ on the mesh is estimated at the vertex $i$ as

$$\Delta\psi|_i = -\psi_i + \frac{1}{|N_1(i)|}\sum_{j\in\mathcal{N}(i)}\psi_j,$$

where $N_1(i)$ denotes the one-ring of $i$, i.e., the set of vertices adjacent to $i$ by an edge. The alternative is to take the eigenfunctions of the Laplace-Beltrami operator on the mesh, as we do in (10) below for solving the biharmonic PDE. However, the advantage of the “simple-minded” approach is that the basis does not change as the model deforms, making it unnecessary to solve a large sparse eigensystem at every iteration of deformable modeling. In practice we have found the current approach to work well, so we took advantage of it’s relative inexpensiveness.

**3.3.3. Numerical Solution of Biharmonic PDE Using Finite Differences—**Glowinski and Pironneau (1979) show that the biharmonic equation on a domain in $\mathbb{R}^2$ can be reduced to a system of harmonic equations by introducing a new unknown variable $\omega = \Delta_{\mathbf{m}}\varphi$ and simultaneously solving for $\varphi$ and $\omega$ By the same token, the biharmonic equation on the medial manifold (7) can be written as a system of two harmonic equations:

$$\begin{aligned}
&\Delta_{\mathbf{m}}\varphi = \omega,\\
&\Delta_{\mathbf{m}}\omega = \rho,\\
&\varphi|_\gamma = \tau^2,\\
&\varphi_{,\nu}|_\gamma = -2\tau\sqrt{1-(\mathrm{d}\tau/\mathrm{d}s)^2},
\end{aligned} \tag{8}$$

Using the finite difference method, this equation reduces to a $(2n \times 2n)$ sparse linear system, where $n$ is the number of vertices in the finite difference mesh. Glowinski and Pironneau

(1979) further reduce this system to an ($n \times n$) sparse linear system and a ($k \times k$) dense linear system, where $k < n$ is the number of vertices at the boundary of the domain. In our implementation we found that solving the ($2n \times 2n$) sparse linear system is sufficiently fast not to require further reduction.

The solution of (8) using the finite difference method is complicated by the fact that the Laplace-Beltrami operator (LBO) is defined on an simplicial surface in $\mathbb{R}^3$ rather than on a planar grid. Many approximations of the LBO have been proposed in the literature. Wardetzky et al. (2007) point out that diversity of proposed operators is due to the fact that no "ideal" digital LBO may be found, i.e., no digital operator may at once satisfy the desirable properties of "symmetry", "locality", "linear precision" and "positive weights". Our solution follows the framework established by Pinkall and Polthier (1993) with robustness modifications by Bobenko and Springborn (2007). This approach satisfies all of the four desired properties except locality (Wardetzky et al., 2007). Since our aim is to get as good an approximation of the solution as possible, the locality property is the easiest to sacrifice.

In general, the LBO is defined on a mesh as a weighted sum

$$(\Delta_{\mathbf{m}}\varphi)_i = \sum_{j \in N_1(i)} w_{ij}(\varphi_j - \varphi_i) \tag{9}$$

where $w_{ij}$ is a weight assigned to each edge in the mesh. Pinkall and Polthier (1993) and later Desbrun et al. (1999) proposed the widely-used *cotan formula* for $w_{ij}$:

$$w_{ij} = \frac{3}{A_i} \frac{\cot \alpha_{ij} + \cot \beta_{ij}}{2}, \tag{10}$$

where $A_i$ is the sum of the areas of the triangles that share the vertex $i$, and $\alpha_{ij}$-, $\beta_{ij}$ are the two angles opposite to the edge ($i$,$j$). This expression has been widely used for Laplacian mesh smoothing, minimum surfaces computation and many other applications. However, the weights $w_{ij}$ can be negative on arbitrary meshes leading to the violation of the maximum principle and other problems (Wardetzky et al., 2007). Bobenko and Springborn (2007) propose an elegant solution to this problem by applying *intrinsic Delaunay triangulation* to the mesh before computing LBO using the *cotan* formula. This approach also ensures that the PDE solution is intrinsic: dependent only on the vertices of the mesh and not on its triangulation. Intrinsic Delaunay triangulation can be performed using an efficient *intrinsic edge flipping* algorithm (Glickenstein, 2005; Fisher et al., 2006), which terminates in finite time and has a unique solution (Bobenko and Springborn, 2007). Our implementation of the finite difference method includes the edge flip algorithm.

In addition to the LBO, to solve (8), we require finite difference approximations of $\varphi_{,\boldsymbol{\nu}}$ and $d\tau/ds$ at vertices that lie at the edges of the medial mesh, where the boundary conditions are defined. We also require an approximation of the Riemannian gradient $\nabla_{\mathrm{m}}\,\varphi$ for the inverse skeletonization expression (2).

To estimate intrinsic first-derivative quantities of some function $f$ on the mesh **m,** we start with expressions for tangents to the Loop subdivision surfaces given by Loop (1987). A pair of tangent vectors $\mathbf{m}_{,1}$, $\mathbf{m}_{,2}$ to the limit surface **m** at vertex $i$ is given by expressions of the form

$$(\mathbf{m}_{,d})_i = w_{ii,d}\,\mathbf{m}_i + \sum_{j\in N_1(i)} w_{ij,d}\,\mathbf{m}_j, \quad d=1,2. \tag{11}$$

The weights $w_{ij,d}$ can be found in the review by Zorin et al. (2000, p.71). Given these tangent vectors, one can compute at each vertex the covariant metric tensor $g_{pq} = \mathbf{m}_{,\mathrm{p}} \cdot \mathbf{m}_{,q}$ and the contravariant metric tensor $g^{pq}$, given by the Einstein notation expression $g^{pq} g_{pq} = \delta^p_q$. The derivatives of $f$ in directions of $\mathbf{m}_{,1}$ and $\mathbf{m}_{,2}$ are similarly given by

$$(f_{,d})_i = w_{ii,d}\,f_i + \sum_{j\in N_1(i)} w_{ij,d}\,f_j, \quad d=1,2, \tag{12}$$

where the weights $w_{ij,d}$ are the same in both expressions. We can obtain the Riemannian gradient of $f$ as

$$\nabla_{\mathbf{m}} f = g^{pq}\,\mathbf{m}_{,p}\,f_{,q},$$

and its squared magnitude as

$$|\nabla_{\mathbf{m}} f|^2 = g^{pq}\,f_{,p}\,f_{,q}.$$

Notice that this expression is non-linear in $f$, so it is unsuitable for finite difference modeling. However, the gradient magnitude, although part of the constraint (3), does not appear in the PDE (8) and this non-linearity does not pose a problem for solving the PDE.

At the vertices along the boundaries and creases of the Loop subdivision surface, $\mathbf{m}_{,1}$ is parallel to $\gamma$, the curve that forms the boundary of the subdivision surface and, thus, perpendicular to the outward normal, $v$. Therefore, $f_{,S}$, where $s$ is the uniform arc length parameterization of $\gamma$, is given by

$$f_{,s} = f_{,1} / \sqrt{g_{11}},$$

and the normal derivative is given by

$$f_{,v} = \frac{g_{11}\,f_{,2} - g_{12}\,f_{,1}}{g_{11}\sqrt{g_{22}}}.$$

Plugging in (12) for $f_{,1}$ and $f_{,2}$ in the above two expressions, we get finite difference expressions for $f_{,S}$ and $f_{,v}$,. Finally, substituting $\tau$ and $\varphi$ for $f$, we obtain the finite difference expressions for all of the terms appearing in the PDE (8).

With the help of finite difference expressions for $\Delta_{\mathbf{m}}\,\varphi$, $\Delta_{\mathbf{m}}\omega$, $\varphi_{,v}$ and $\tau_{,s}$, the PDE (8) reduces to the linear system

$$A\begin{bmatrix}\varphi\\ \omega\end{bmatrix}=b, \tag{13}$$

where $A$ is a sparse matrix. However, the matrix $A$ may not be of full rank. The reason this happens is that $\varphi$ is fixed at the boundary nodes by the Dirichlet boundary conditions, so the boundary condition involving $\varphi_{,v}$ imposes constraints on the values of $\varphi$ "just inside" of the boundary. If there are fewer values to satisfy these constraints than there are constraints, the problem will not have a solution. To avoid this problem, we ensure that the meshes used to represent medial manifolds have more vertices just inside of the boundary than there are boundary vertices. To solve the sparse linear system, we use the direct solver PARDISO (Schenk and Gärtner, 2004).

### 3.4. Medial Coordinate System

A key property of cm-rep medial models is the ability to parameterize the entire interior of the model using a shape-based coordinate system. First, suppose that the medial manifold **m** is parameterized by a vector $\mathbf{u} = (u^1, u^2)$. Recall from Sec. 2.3 that every point $\mathbf{m}(\mathbf{u})$ on the medial manifold is mapped by inverse skeletonization (1) to a pair of points $\mathbf{b}^+(\mathbf{u})$ and $\mathbf{b}^-(\mathbf{u})$, which coincide if $\mathbf{m}(\mathbf{u})$ is at an edge of the medial manifold. We refer to the line segments $S^+(\mathbf{u}) = \{\mathbf{m}(\mathbf{u}),\mathbf{b}^+(\mathbf{u})\}$ and $S^-(\mathbf{u}) = \{\mathbf{m}(\mathbf{u}),\mathbf{b}^-(\mathbf{u})\}$ as *spokes.* When the sufficient constraints of inverse skeletonization are met, the spokes span the interior of the model, i.e., every point in the region enclosed by the surface $\mathbf{b}^-\cup\mathbf{b}^+$ belongs to exactly one spoke, except for the obvious case of spokes originating at medial manifold edges, where $S^+(\mathbf{u}) = S^-(\mathbf{u})$. Let us use the coordinate $\xi \in [-1,1]$ to describe a location along a spoke (when $\xi > 0$, it references the spoke $S^+$, and when $\xi < 0$, it references the spoke $S^-$). Then every point **x** on the model's interior can be assigned a set of coordinates $(\mathbf{u}, \xi)$, as follows:

$$\mathbf{x}(u,v,\xi)=\begin{cases}\mathbf{m}(\mathbf{u})+\xi R(\mathbf{u})\,U^+(\mathbf{u}) & \text{if } \xi \geq 0\\ \mathbf{m}(\mathbf{u})-\xi R(\mathbf{u})U^-(\mathbf{u}) & \text{otherwise.}\end{cases} \tag{14}$$

This assignment is unique, except at manifold edges, as noted above.

Fig. 4 illustrates the concept of this coordinate system in two dimensions. This parametrization of the cm-rep model interior is a powerful tool. In image matching applications, it allows image data to be sampled over the interior of a model in an efficient and natural way, without having to worry about sampling the same point in image space twice. When matching binary objects, this ability allows us to optimize overlap between the model and the target object, something that is not as straightforward for boundary-based deformable models. The coordinate system also makes it possible to establish volumetric shape-based correspondences between different instances of an anatomical structure and serves as the basis of *shape-based normalization* (Yushkevich et al., 2007).

### 3.5. Deformable Modeling

In most applications, cm-rep deformable modeling involves maximizing the overlap between the deforming model and a binary segmentation of the given target structure. Although there has been plenty of work on using medial representations to segment anatomical structures directly in medical images (Stough et al., 2007; Pizer et al., 2005; Rao et al., 2005; Pizer et al., 2003a), segmentation is not the focus of our paper. Other applications of continuous medial models include shape-based normalization (Yushkevich et al., 2007), shape analysis (Sun et al., 2008b) and data dimensionality reduction (Yushkevich et al., 2008). For these applications,

we typically start with a given segmentation of the structure of interest and require to fit a medial model to it.

The problem of fitting cm-rep models to anatomical structures is described in earlier work (Yushkevich et al., 2006, Sec. III-F). There are essentially no differences in terms of the objective function between the biharmonic cm-rep model and the earlier Poisson-based model. Model fitting involves numerical optimization, where the objective function consists of an image match term (Dice overlap), a regularization prior, and penalties terms used to ensure that the *inequality constraints* required for inverse skeletonization are met. These constraints include requiring that the solution $\varphi$ of the biharmonic PDE be positive (since $R = \sqrt{\varphi}$), that $|\nabla_{\mathbf{m}} R| \leq 1$, and that the surface $\mathbf{b}^+ \cup \mathbf{b}^-$ not self-intersect. The latter can typically be satisfied locally by imposing a penalty on the Jacobian of the **U** vector field in (2). Regularization priors are used to maintain geometrical correspondence when models are fitted to multiple instances of an anatomical structure. A simple regularization prior is penalizes the gradient magnitude of the determinant of the metric tensor the mapping between the deforming model and a target model. Optimization uses the Gay (1983) model/trust region based approach.

## 4. Experiments and Results

The aims of this experimental section are (1) to illustrate the ability of cm-rep models to accurately represent natural variability in the shape of anatomical structures; (2) to demonstrate the capacity to perform linear statistical analysis in the space of cm-rep models.

The motivation for the first aim is that cm-rep models are, by construction, a lossy representation for anatomical structures. The branching topology of the skeleton of a cm-rep model is maintained during deformable modeling. Since real-world variability in the topology of the skeletons of anatomical structures is vast, cm-reps can only fit target anatomy approximately. However, it has been found, both in the case of discrete (Styner et al., 2003a) and continuous medial models (Yushkevich et al., 2006, 2008; Sun et al., 2008a), that for some structures, such as the hippocampus, the approximation error is quite small, especially when compared with errors associated with manually or automatically segmenting these structures from anatomical images. In this paper, we again carry out fitting accuracy analysis to ensure that cm-rep models based on the biharmonic PDE perform as well or better than earlier approaches.

The second experimental aim shows off the particular advantages of PDE-based medial modeling. It takes advantage of the fact that the PDE creates a diffeomorphic mapping from a parameter space that is a codimension-0 subset of $\mathbb{R}^N$ to the space of "valid" cm-rep models. This mapping allows us to apply linear operations, such as principal component analysis (PCA), linear discrimination, or shape interpolation to cm-rep parameters and to generate new "valid" cm-rep instances. Without the PDE, linear combination of cm-rep models would lead to "invalid" instances, because nonlinear equality constraints (3) and (4) would be violated.

### 4.1. Hippocampus

**4.1.1. Subjects, Imaging and Data Processing—**The dataset used in this experiment was graciously provided to us by Prof. Guido Gerig (Department of Computer Science, University of Utah) and Prof. Sarang Joshi (Departments of Biomedical Engineering and Bioengineering, University of Utah). The data includes 1.5 Tesla T1-weighted SPGR MRI scans ($0.9375 \times 0.9375 \times 1.5\text{mm}^3$ voxel size) for 87 subjects from a previously published schizophrenia study (Chakos et al., 2005); the subjects included patients with early illness and chronic disease, as well as controls matched by age and gender. The dataset also includes left and right hippocampus segmentations, obtained automatically using the Joshi et al. (1997) large deformation diffeomorphic registration method that incorporates expert-placed anatomic

landmarks. This segmentation approach is used extensively in brain morphometry (Csernansky et al., 1998) and was shown to have greater interrater reliability than manual segmentation (Haller et al., 1997). This data has been analyzed previously using statistical features derived from boundary and discrete medial representations, and differences in the shape and size of the hippocampus between schizophrenia patients and controls were detected (Styner et al., 2003b; Gerig et al., 2002, 2003).

Hippocampus segmentations were provided in the form of high-resolution boundary surface meshes. We scan-converted and flood-filled these meshes to generate binary masks with the voxel size $0.33mm^3$. An initial medial model was constructed using a skeletonization and flattening based procedure described in an earlier paper (Yushkevich et al., 2008, Sec. 3.4.1). The model has 6336 triangles and 3289 vertices. Model fitting followed a multi-resolution schedule, with the first level performing affine alignment, and the next three levels performing deformable modeling using 10, 40 and 120 Laplace eigenfunctions (see Sec. 3.3.2).

**4.1.2. CM-Rep Fitting Accuracy—**Fitting accuracy was evaluated in terms of overlap and distance between the model's boundary and target structure's boundary. Overlap between a fitted cm-rep model and the target hippocampus mask was measured using *Dice similarity coefficient* (Dice, 1945), a symmetric overlap measure frequently used to compare agreement between segmentations (*e.g.*, (Zou et al., 2004)). Boundary-based criteria describe the average (as well as maximal) distance from the fitted cm-rep models to the corresponding hippocampus meshes and, *vice versa*, from the hippocampus meshes to the fitted cm-rep models (average and maximal mesh-to-mesh distance is asymmetrical). The means of these maximal and average distances over all subjects are reported in Table 1, with earlier results on the same dataset from (Yushkevich et al., 2006) listed for comparison. These earlier results were generated using the previous generation cm-rep approach, where the Poisson PDE with non-linear boundary conditions was used instead of the bi-harmonic PDE and the medial model was defined on a rectangular grid rather than on an arbitrary triangle mesh. The newer generation cm-rep model performs markedly better than the old model. Particularly encouraging is the improvement in maximal distance between the cm-rep model and the target boundary, which decreased by about 0.2mm with the new cm-rep model. The improvement over earlier work is most likely attributable to freeform triangular meshing used in the current approach (we were unsuccessful in implementing the non-linear Poisson-based approach on triangular meshes due to convergence failures).

**4.1.3. Vector Space Statistical Analysis—**To illustrate the ability to perform linear statistical analysis on cm-rep models satisfying the equality constraint (3), we perform principal component analysis using models fitted to the left hippocampus in all 89 subjects following alignment by generalized Procrustes algorithm (Gower, 1975). PCA is computed in a straightforward manner, combining the values of $\mathbf{m}$, $\rho$ and $\tau$ at each vertex into a single coefficient vector. In practical applications, $\rho$ and $\tau$ should be treated differently from $\mathbf{m}$, but we believe that for a proof of concept demonstration, the current approach suffices. Fig. 6 shows the cm-rep models corresponding to the mean of the coefficient vectors and to the first 3 principal components. Although all cm-rep models generated by the PDE satisfy the equality constraint (3) at the boundary, other inequality constraints may be violated by the generated models. For example, the model sampled at −3 standard deviations along the first principal component has $\varphi < 0$ at some vertices, leading to an invalid cm-rep model.

**4.1.4. Convergence—**We use the hippocampus dataset to demonstrate that cm-rep models converge to a continuous limit. Using data from the first 15 subjects, we start with a model containing 853 vertices in the medial manifold mesh, and apply Loop subdivision three times, resulting in a model with over 50000 vertices. Table 2 reports differences in $\varphi$, $R$, $|\nabla \mathbf{m} R|$ and $\mathbf{b}$ between models at the three coarser scales and the finest scale model. The convergence is

slightly better than linear with respect to edge length, which goes down by the factor of two at each subdivision.

### 4.2. White Matter Structures

CM-reps have applications beyond modeling subcortical structures. In an recent paper (Yushkevich et al., 2008), we used cm-rep models to represent white matter fasciculi with more complex shapes, including the corpus callosum and the corticospinal tract. The structures were segmented by performing fiber tractography (Mori et al., 2002) in a white matter atlas generated using deformable registration of diffusion tensor images (Zhang et al., 2007) from a chromosome DS22q11.2 deletion study (Simon et al., 2008). The cm-rep approach we previously used to model these structures does not use a PDE; instead we simply admitted skeleton meshes that slightly violated the equality constraint and corrected these solutions by local adjustment. The advantage of the PDE-based approach is that it allows linear operations on cm-rep models, such as the PCA illustrated in a previous section. Fig. 7 shows biharmonic PDE-based cm-rep models fitted to the corpus callosum and the corticospinal tract segmentations. The Dice overlap for these more complex structures is 0.92 and 0.94, respectively. Some of the complexities of the shapes are not captured, but the overall fit is very close.

## 5. Discussion and Conclusions

### 5.1. Contributions

This work represents a second-generation PDE-based deformable medial model that offers several distinct advantages over earlier work (Yushkevich et al., 2006) that used a non-linear Poisson PDE. The additional degree of freedom that the biharmonic PDE offers allows us to incorporate medial geometric constraints as *linear* boundary conditions. Issues of poor convergence that prevented us from implementing the Poisson model on arbitrary triangular meshes are thus resolved, and an additional benefit is the ability to generalize to branching medial models. The biharmonic model retains the main advantages of the original Poisson model: (1) the ability to faithfully represent the geometric relationship between the skeleton and the boundary of a deformable model; (2) the ability to map linear combinations of parametric representations of such models into the space of valid models; and (3) the ability to closely capture the variability in the shape of anatomical structures, particularly, the hippocampus.

### 5.2. Limitations

Although the biharmonic model simplifies medial modeling significantly, a number of issues remain to be resolved. Whereas the equality constraints for inverse skeletonization are neatly enforced by the PDE, inequality constraints still have to be enforced, which is done rather inefficiently by introducing penalty functions into the optimization. These constraints pose a challenge to linear interpolation of cm-rep models, even though for the hippocampus dataset, constraint violations do not arise until one moves about 3 standard deviations from the mean.

The finite differences approach used to implement the biharmonic equation may also be subject to improvement. Although remeshing using Delaunay flips helps ensure numerical stability, issues with the convergence of a model to the limit still arise. For more complex models, such as the corpus callosum, a model fitted at a given resolution may have $\varphi > 0$ everywhere, whereas the limit of $\varphi$, as the resolution of the mesh increases, may be negative. A more sophisticated numerical method may help resolve this issue. Another workaround, which remains to be explored, may be to ensure that the solution is always positive by framing $R$ as an exponential function of $\varphi$, rather than $R = \sqrt{\varphi}$, as we do currently.

### 5.3. Generalization to Branching Medial Geometry

One of the conceptual advantages of the medial model based on the biharmonic PDE is the ability to generalize to branching skeletons, which was not the case for the earlier Poisson-based cm-rep model. Along the seams in a branching medial model, the equality constraint (4) must hold at every point. This constraint can be rewritten in terms of the derivative of $R$ in the direction of $\nu$, the outward unit normal vector along the seam curve $\gamma(s)$. There are three such constraints, one for each of the medial manifolds $\mathbf{m}_1$, $\mathbf{m}_2$, $\mathbf{m}_3$ coming together at the seam:

$$R_{,\nu_i}|_\gamma = \sqrt{1-(R_{,s})^2}\cos\alpha_i, \tag{15}$$

where $\alpha_i$ is the angle between the tangent planes of the medial manifolds $\mathbf{m}_{i\oplus 1}$ and $\mathbf{m}_{i\oplus 2}$, i.e.,

$$\cos\alpha_i = \nu_{i\oplus 1}\cdot\nu_{i\oplus 2},$$

with $\oplus$ denoting addition modulo 3.

Let us split the branching medial skeleton along the seams, breaking it up into several manifolds, each bounded by edges and seams of the original skeleton (this operation may create manifolds with infinitely thin holes, but we can still treat them as boundaries). Let $\gamma_{\text{seam}}$ and $\gamma_{\text{edge}}$ be the boundaries of these manifolds. Then on each of these manifolds we can define a biharmonic PDE that incorporates the seam equality constraint (15) and the edge equality constraint (5):

$$\begin{aligned}
&\Delta^2_{\mathbf{m}}\varphi = \rho,\\
&\varphi|_\gamma = \tau^2,\\
&\varphi_{,\nu}|_{\gamma_{\text{seam}}} = 2\tau\sqrt{1-(\mathrm{d}\tau/\mathrm{d}s)^2}\,\nu_{i\oplus 1}\cdot\nu_{i\oplus 2},\\
&\varphi_{,\nu}|_{\gamma_{\text{edge}}} = -2\tau\sqrt{1-(\mathrm{d}\tau/\mathrm{d}s)^2}.
\end{aligned} \tag{16}$$

Each seam curve in the original skeleton appears three times in the set of manifold-specific biharmonic equations that we define. The function $\tau$ must be the same along a given seam curve in each of the equations in which it appears; otherwise, the solution $\varphi$ would be discontinuous at the seam.

Note that this simple solution is possible for the fourth order biharmonic PDE that admits both a zeroth-order and a first-order boundary condition. With a second order PDE, which admits only one boundary condition, we can still specify the constraint on $\varphi,\boldsymbol{\nu}\,|\,\gamma_{seam}$, but the value of the solution $\varphi$ along the seam will be different in each of the three manifolds that share the seam, creating a discontinuity across the seam!

Fig. 8 shows a toy example where the biharmonic PDE is applied to a branching skeleton. The skeleton is formed by rotational extrusion of a two-dimensional branch shaped as an upside down letter "Y". Constant values of $\tau$ are prescribed along the medial seam and the three medial edges and $\rho = 0$ is given on each of the manifolds. The biharmonic PDE (16) is solved on each of the manifolds, giving a radius function $R$ that is continuous across the seam. Inverse skeletonization (1) gives a closed boundary surface.

Our examination of medial branching with the biharmonic equation is intended as a proof of concept and does not take into account the additional equality constraint at the points where

seams and edges intersect (the toy example does not have these intersections). This constraint must be incorporated in order to model real-world anatomical structures with branching skeletons. This remains the subject of future work.

## Acknowledgements

This work was supported by the NIH grants NS061111 (PY) and AG027785 (PY). We gratefully acknowledge Prof. Guido Gerig, of the Department of Computer Science at the University of Utah, and Prof. Sarang Joshi, of the Departments of Biomedical Engineering and Bioengineering at the University of Utah, and their colleagues for providing the hippocampus segmentations used in this work. We thank Dr. Tony J. Simon, of the Department of Psychiatry and Behavioral Sciences, M.I.N.D. Institute, University of California, Davis, for providing the imaging data used in the white matter experiments.

## References

Belkin M, Niyogi P. Laplacian eigenmaps for dimensionality reduction and data representation. Neural Computation 2003;15(6):1373–1396.

Biermann, H.; Levin, A.; Zorin, D. Piecewise smooth subdivision surfaces with normal control; Proceedings of SIGGRAPH 2000; 2000. p. 113-120.

Blum, H. Models for the Perception of Speech and Visual Form. MIT Press; 1967. A transformation for extracting new descriptors of shape.

Bobenko AI, Springborn BA. A discrete Laplace-Beltrami operator for simplicial surfaces. Discrete Comput Geom 2007;38(4):740–756.

Bouix S, Pruessner JC, Collins DL, Siddiqi K. Hippocampal shape analysis using medial surfaces. Neuroimage 2005;25(4):1077–89. [PubMed: 15850726]

Chakos MH, Schobel SA, Gu H, Gerig G, Bradford D, Charles C, Lieberman JA. Duration of illness and treatment effects on hippocampal volume in male patients with schizophrenia. Br J Psychiatry 2005;186:26–31. [PubMed: 15630120]

Chung MK, Robbins SM, Dalton KM, Davidson RJ, Alexander AL, Evans AC. Cortical thickness analysis in autism with heat kernel smoothing. Neuroimage 2005;25(4):1256–1265. [PubMed: 15850743]

Crouch JR, Pizer SM, Chaney EL, Hu YC, Mageras GS, Zaider M. Automated finite-element analysis for deformable registration of prostate images. IEEE Trans Med Imaging 2007;26(10):1379–1390. [PubMed: 17948728]

Csernansky J, Joshi S, Wang L, Haller J, Gado M, Miller J, Grenander U, Miller M. Hippocampal morphometry in schizophrenia via high dimensional brain mapping. Proc National Academy of Sciences 1998;95:11406–11411.

Damon J. On the smoothness and geometry of boundaries associated to skeletal structures I: Sufficient conditions for smoothness. Annales Inst Fourier 2003;53:1941–1985.

Damon J. On the smoothness and geometry of boundaries associated with skeletal structures II: Geometry in the Blum case. Compositio Mathematica 2004;140(6):1657–1674.

Damon J. Determining the geometry of boundaries of objects from medial data. International Journal of Computer Vision 2005;63(l):45–64.

Desbrun, M.; Meyer, M.; Schroeder, P.; Barr, AH. SIGGRAPH ’99. ACM Press/Addison-Wesley Publishing Co.; New York, NY, USA: 1999. Implicit fairing of irregular meshes using diffusion and curvature flow; p. 317-324.

Dice LR. Measures of the amount of ecologic association between species. Ecology 1945;26(3):297–302.

Fisher, M.; Springborn, B.; Bobenko, AI.; Schroder, P. SIGGRAPH ’06: ACM SIGGRAPH2006 Courses. ACM; New York, NY, USA: 2006. An algorithm for the construction of intrinsic delaunay triangulations with applications to digital geometry processing; p. 69-74.

Gay DM. Algorithm 611: Subroutines for unconstrained minimization using a model/trust-region approach. ACM Transactions on Mathematical Software 1983;9(4):503–524.

Gerig G, Muller KE, Kistner EO, Chi Y, Chakos M, Styner M, Lieberman JA. Age and treatment related local hippocampal changes in schizophrenia explained by a novel shape analysis method. Medical Image Computing and Computer-Assisted Intervention, MICCAI. 2003

Gerig, G.; Styner, M.; Chakos, M.; Lieberman, J. Hippocampal shape alterations in schizophrenia: results of a new methodology. Proc. 11th Biennial Workshop on Schizophrenia; 2002.

Giblin P, Kimia BB. A formal classification of 3D medial axis points and their local geometry. IEEE Trans Pattern Anal Mach Intell 2004;26(2):238–51. [PubMed: 15376898]

Giblin PJ, Kimia BB. On the intrinsic reconstruction of shape from its symmetries. IEEE Transactions on Pattern Analysis and Machine Intelligence 2003;25(7):895–911.

Glickenstein D. Geometric triangulations and discrete laplacians on manifolds. 2005arXiv:math.MG/0508188

Glowinski R, Pironneau O. Numerical methods for the first biharmonic equation and for the two-dimensional Stokes problem. SIAM Review 1979;21(2):167–212.

Golland, P.; Grimson, W.; Kikinis, R. International Conference on Information Processing in Medical Imaging. Vol. 1613. Springer Verlag; 1999. Statistical shape analysis using fixed topology skeletons: corpus callosum study; p. 382-388.LNCS

Gower J. Generalized procrustes analysis. Psychometrika 1975;40:33–51.

Haller J, Banerjee A, Christensen G, Gado M, Joshi S, Miller M, Sheline Y, Vannier M, Csernansky J. Three-dimensional hippocampal MR morphometry by high-dimensional transformation of a neuroanatomic atlas. Radiology 1997;202:504–510. [PubMed: 9015081]

Joshi S, Grenander U, Miller M. On the geometry and shape of brain sub-manifolds. IEEE Transactions on Pattern Analysis and Machine Intelligence 1997;11:1317–1343.

Joshi S, Pizer S, Fletcher PT, Yushkevich P, Thall A, Marron JS. Multiscale deformable model segmentation and statistical shape analysis using medial descriptions. IEEE Trans Med Imaging 2002;21(5):538–550. [PubMed: 12071624]

Kami, Z.; Gotsman, C. SIGGRAPH '00: Proceedings of the 27th annual conference on Computer graphics and interactive techniques. ACM Press/Addison-Wesley Publishing Co.; New York, NY, USA: 2000. Spectral compression of mesh geometry; p. 279-286.

Kimia B, Tannenbaum A, Zucker S. Shape, shocks, and deformations I: the components of two-dimensional shape and the reaction-diffusion space. International Journal of Computer Vision 1995;15:189–224.

Loop, C. Master's thesis. Department of Mathematics, University of Utah; Salt Lake City: 1987. Smooth subdivision surfaces based on triangles.

Mori S, Kaufmann WE, Davatzikos C, Stieltjes B, Amodei L, Fredericksen K, Pearlson GD, Melhem ER, Solaiyappan M, Raymond GV, Moser HW, van Zijl PCM. Imaging cortical association tracts in the human brain using diffusion-tensor-based axonal tracking. Magn Reson Med 2002;47(2):215–223. [PubMed: 11810663]

Nackman, LR. Phd thesis. University of North Carolina; Chapel Hill: 1982. Three-dimensional shape description using the symetric axis transform. Department of Computer Science

Näf, M.; Kübler, O.; Kikinis, R.; Shenton, M.; Székely, G. Characterization and recognition of 3D organ shape in medical image analysis using skeletonization. Workshop on Mathematical Methods in Biomedical Image Analysis; IEEE Computer Society; 1996. p. 139-150.

Ogniewicz RL, Kübler O. Hierarchic Voronoi skeletons. Pattern Recognition 1995;28(3):343–359.

Pinkall U, Polthier K. Computing discrete minimal surfaces and their conjugates. Experimental Mathematics 1993;2:15–36.

Pizer SM, Fletcher PT, Joshi S, Gash AG, Stough J, Thall A, Tracton G, Chaney EL. A method and software for segmentation of anatomic object ensembles by deformable m-reps. Med Phys 2005;32(5):1335–1345. [PubMed: 15984685]

Pizer SM, Fletcher PT, Joshi S, Thall A, Chen JZ, Fridman Y, Fritsch DS, Gash AG, Glotzer JM, Jiroutek MR, Lu C, Muller KE, Tracton G, Yushkevich P, Chaney EL. Deformable m-reps for 3D medical image segmentation. International Journal of Computer Vision 2003a;55(2):85–106.

Pizer SM, Siddiqi K, Székely G, Damon JN, Zucker SW. Multiscale medial loci and their properties. International Journal of Computer Vision 2003b;55(2–3):155–179.

Qiu A, Bitouk D, Miller MI. Smooth functional and structural maps on the neocortex via orthonormal bases of the laplace-beltrami operator. IEEE Trans Med Imaging 2006;25(10):1296–1306. [PubMed: 17024833]

Rao M, Stough J, Chi YY, Muller K, Tracton G, Pizer SM, Chaney EL. Comparison of human and automatic segmentations of kidneys from ct images. Int J Radiat Oncol Biol Phys 2005;61(3):954–960. [PubMed: 15708280]

Rustamov, RM. SGP '07: Proceedings of the fifth Eurographics symposium on Geometry processing. Eurographics Association; Aire-la-Ville, Switzerland, Switzerland: 2007. Laplace-beltrami eigenfunctions for deformation invariant shape representation; p. 225-233.

Schenk O, Gärtner K. Solving unsymmetric sparse systems of linear equations with PARDISO. Journal of Future Generation Computer Systems 2004;20(3):475–487.

Siddiqi K, Ahokoufandeh A, Dickinson S, Zucker S. Shock graphs and shape matching. International Journal of Computer Vision 1999a;1(35):13–32.

Siddiqi, K.; Bouix, S.; Tannenbaum, A.; Zucker, SW. Proc Computer Vision. Vol. 2. IEEE; 1999b. The hamilton-jacobi skeleton; p. 828-834.

Simon TJ, Wu Z, Avants B, Zhang H, Gee JC, Stebbins GT. Atypical cortical connectivity and visuospatial cognitive impairments are related in children with chromosome 22q11.2 deletion syndrome. Behavioral and Brain Functions 2008;4(25)In press

Stough JV, Broadhurst RE, Pizer SM, Chaney EL. Regional appearance in deformable model segmentation. Inf Process Med Imaging 2007;20:532–543. [PubMed: 17633727]

Styner M, Gerig G, Joshi S, Pizer S. Automatic and robust computation of 3D medial models incorporating object variability. International Journal of Computer Vision 2003a;55(2):107–122.

Styner M, Gerig G, Lieberman J, Jones D, Weinberger D. Statistical shape analysis of neuroanatomical structures based on medial models. Med Image Anal 2003b;7(3):207–20. [PubMed: 12946464]

Styner M, Lieberman JA, Pantazis D, Gerig G. Boundary and medial shape analysis of the hippocampus in schizophrenia. Med Image Anal 2004;8(3):197–203. [PubMed: 15450215]

Sun, H.; Avants, B.; Frangi, A.; Ordas, S.; Gee, J.; Yushkevich, P. IEEE International Symposium on Biomedical Imaging: Macro to Nano. 2008a. Branching medial models for cardiac shape representation. To appear

Sun H, Avants B, Frangi A, Ordas S, Gee JC, Yushkevich P. Cardiac medial modeling and time-course heart wall thickness analysis. Med Image Comput Comput Assist Interv. 2008bAccepted

Terriberry, TB.; Gerig, G. A continuous 3-d medial shape model with branching. International Workshop on Mathematical Foundations of Computational Anatomy MFCA-2006, in conjunction with MIC-CAI 2006; 2006.

Thompson, P.; Hayashi, K.; de Zubicaray, G.; Janke, A.; Rose, S.; Semple, J.; Hong, M.; Herman, D.; Gravano, D.; Dittmer, SDMD.; Toga, A. Improved detection and mapping of dynamic hippocampal and ventricular change in Alzheimers disease using 4D parametric mesh skeletonization. 9th Annual Meeting of the Organization for Human Brain Mapping; 2003.

Thompson PM, Hayashi KM, Sowell ER, Gogtay N, Giedd JN, Rapoport JL, de Zubicaray GI, Janke AL, Rose SE, Semple J, Doddrell DM, Wang Y, van Erp TGM, Cannon TD, Toga AW. Mapping cortical change in alzheimer's disease, brain development, and schizophrenia. Neuroimage 2004;23 (Suppl 1):S2–18. [PubMed: 15501091]

Vermeer, PJ. Phd thesis. Purdue University; 1994. Medial axis transform to boundary representation conversion.

Wardetzky, M.; Mathur, S.; Kälberer, F.; Grinspun, E. SGP '07: Proceedings of the fifth Eurographics symposium on Geometry processing. Eurographics Association; Aire-la-Ville, Switzerland, Switzerland: 2007. Discrete laplace operators: no free lunch; p. 33-37.

Yushkevich P, Fletcher PT, Joshi S, Thall A, Pizer SM. Continuous medial representations for geometric object modeling in 2D and 3D. Image and Vision Computing 2003;21(1):17–28.

Yushkevich PA, Detre JA, Mechanic-Hamilton D, Fernndez-Seara MA, Tang KZ, Hoang A, Korczykowski M, Zhang H, Gee JC. Hippocampus-specific fmri group activation analysis using the continuous medial representation. Neuroimage 2007;35(4):1516–1530. [PubMed: 17383900]

Yushkevich PA, Zhang H, Gee J. Continuous medial representation for anatomical structures. IEEE Trans Med Imaging 2006;25(2):1547–1564. [PubMed: 17167991]

Yushkevich PA, Zhang H, Simon TJ, Gee JC. Structure-specific statistical mapping of white matter tracts. Neuroimage 2008;41(2):448–461. [PubMed: 18407524]

Zhang H, Avants BB, Yushkevich PA, Woo JH, Wang S, McCluskey LF, Elman LB, Melhem ER, Gee JC. High-dimensional spatial normalization of diffusion tensor images improves the detection of white matter differences: an example study using amyotrophic lateral sclerosis. IEEE Trans Med Imaging 2007;26(11):1585–1597. [PubMed: 18041273]

Zorin, D.; Schröder, P.; Derose, T.; Kobbelt, L.; Levin, A.; Sweldens, W. SIGGRAPH Course Notes. ACM; New York: 2000. Subdivision for modeling and animation.

Zou KH, Warfield SK, Bharatha A, Tempany CMC, Kaus MR, Haker SJ III, WMW, Jolesz FA, Kikinis R. Statistical validation of image segmentation quality based on a spatial overlap index. Academic Radiology 2004;11(2):178–189. [PubMed: 14974593]

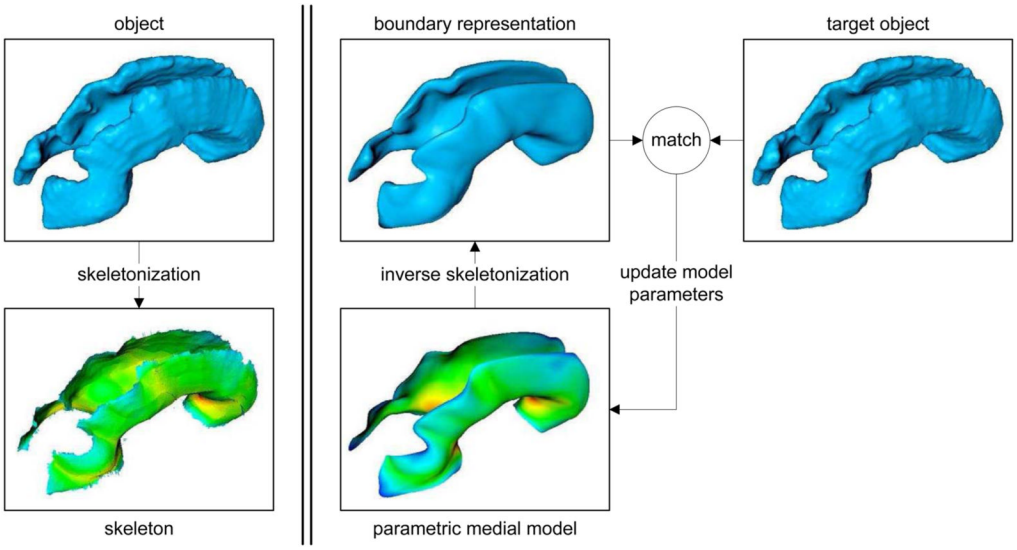


**Fig. 1.**

Skeletonization vs. medial modeling. Left: A 3D object and the skeleton derived by skeletonization. The color map on the skeleton is the "radius scalar field" *R* or, equivalently, the distance to the closest boundary point. Right: medial modeling, which is, essentially, the opposite of skeletonization. A deformable parametric medial model is defined as a surface or set of surfaces, and the boundary is derived analytically using "inverse skeletonization," (see Eqn. 2). The model is then deformed to maximize fit between its boundary and the object of interest. The key difference between skeletonization and medial modeling is that the former computes exact skeletons, but does not guarantee that the branching topology of the skeletons is consistent across individuals; the latter computes approximate skeletons, but guarantees the same topology for all individuals, allowing effective statistical analysis.

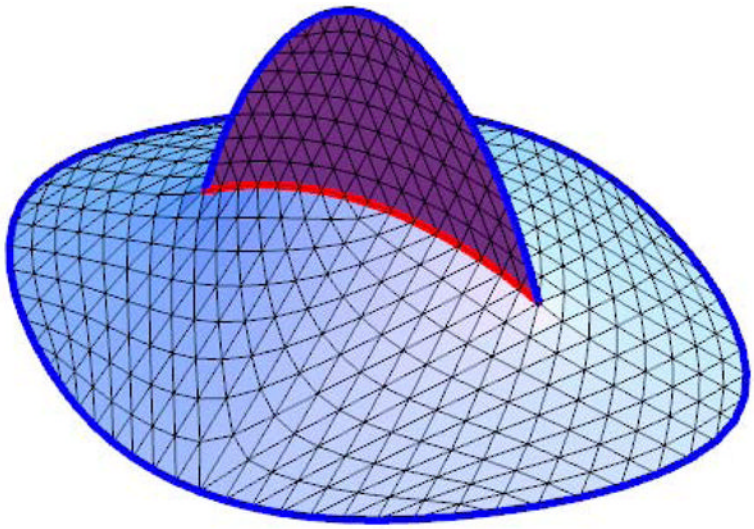

**Fig. 2.**
Example of a branching skeleton. The blue curves forming the outer boundaries of medial manifolds are called *medial edges* and the red curve where the three medial manifolds join is the *medial seam.*

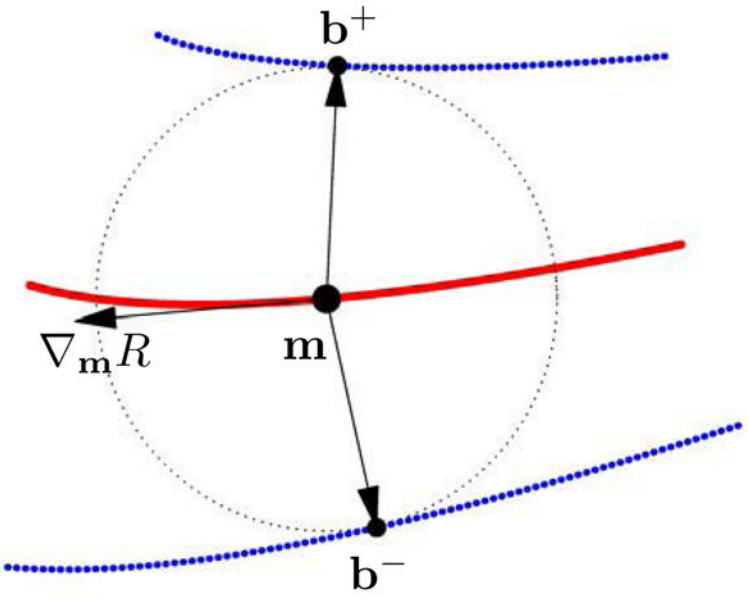


**Fig. 3.**

Two-dimensional diagram of medial geometry. The red curve represents the medial surface (skeleton) **m**. The circle has radius *R*, given by the radial scalar field on **m**. The boundary, shown in blue, consists of two parts, $\mathbf{b}^+$ and $\mathbf{b}^-$, derived from the skeleton and radial scalar field by inverse skeletonization (2). The vector $\nabla_{\mathrm{m}} R$ lies in the tangent plane of **m** and points in the direction of greatest change in *R*. The arrows pointing from **m** to $\mathbf{b}^+$ and $\mathbf{b}^-$ are called *spokes*.

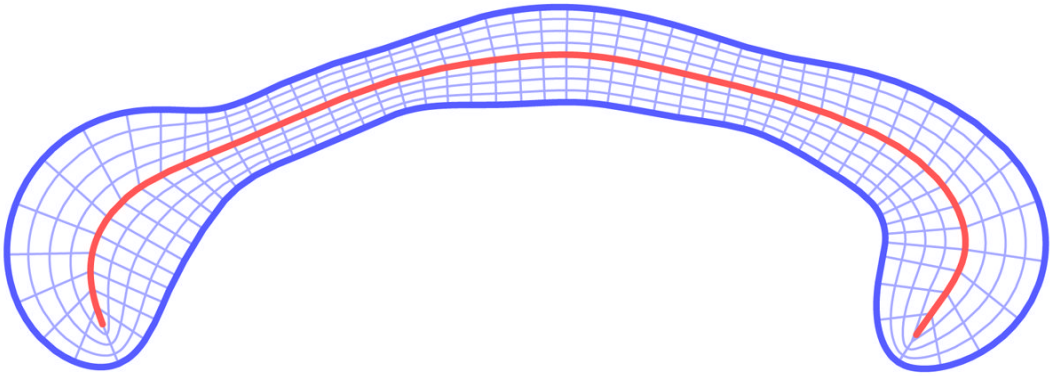

**Fig. 4.**

Medial coordinate system (in 2D). The skeleton forms one axis, and the spokes, projecting from the skeleton to the boundary (orthogonally to the latter) form the second axis. Each point inside the model is has a unique coordinate value. The medial coordinate system extends the parameterization of the skeleton onto the whole interior of the object, providing a way to compute shape-based correspondences between similar objects.

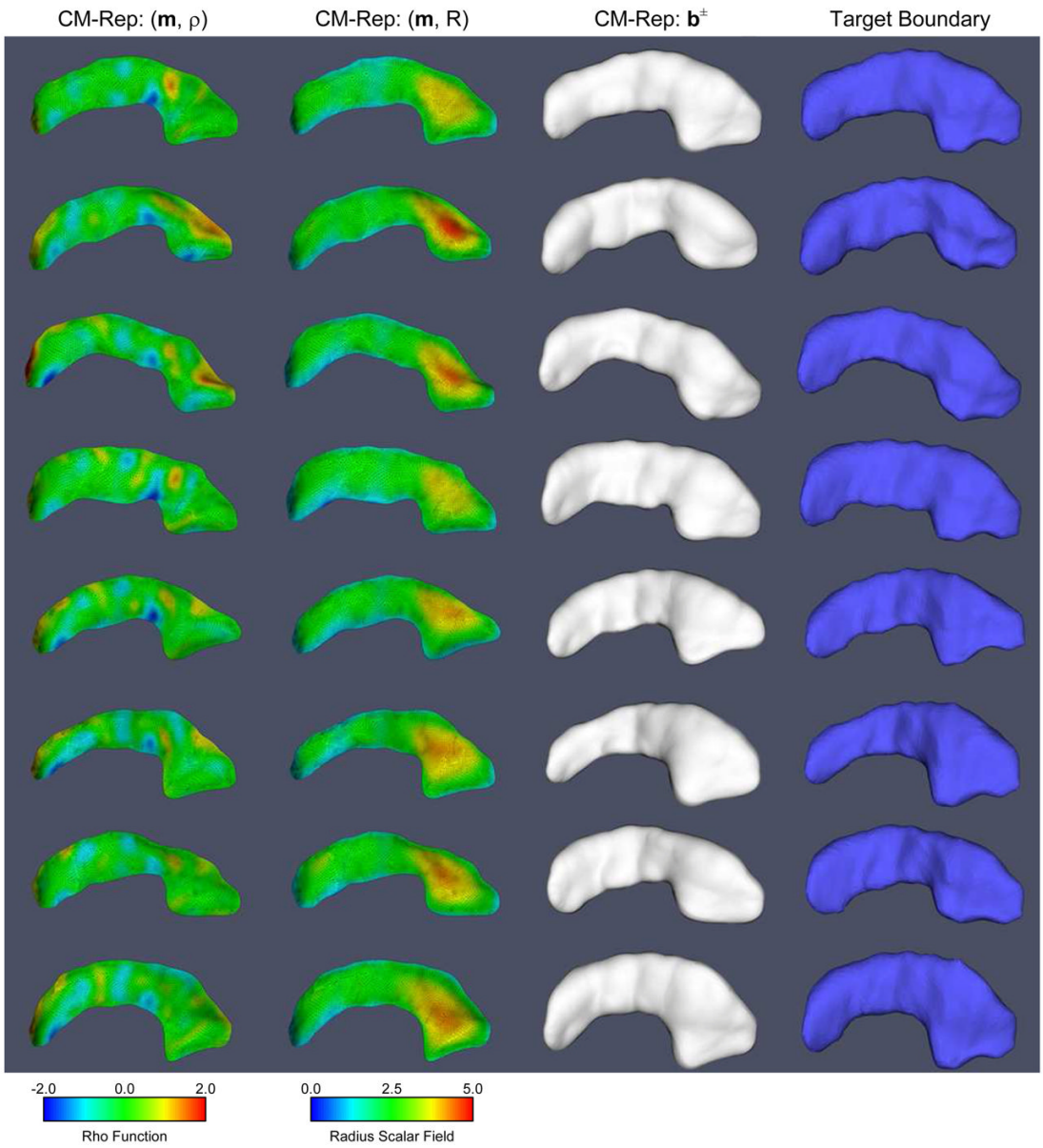


**Fig. 5.**

Examples of cm-rep models fitted to binary segmentaions in the hippocampus dataset. For each hippocampus, shown are the medial manifold colored by the $\rho$ function (the right hand side of the biharmonic PDE), the medial manifold colored by the radius function $R$ (the solution of the PDE), the boundary generated by inverse skeletonization (1), and the boundary of the segmentation to which the cm-rep was fitted.

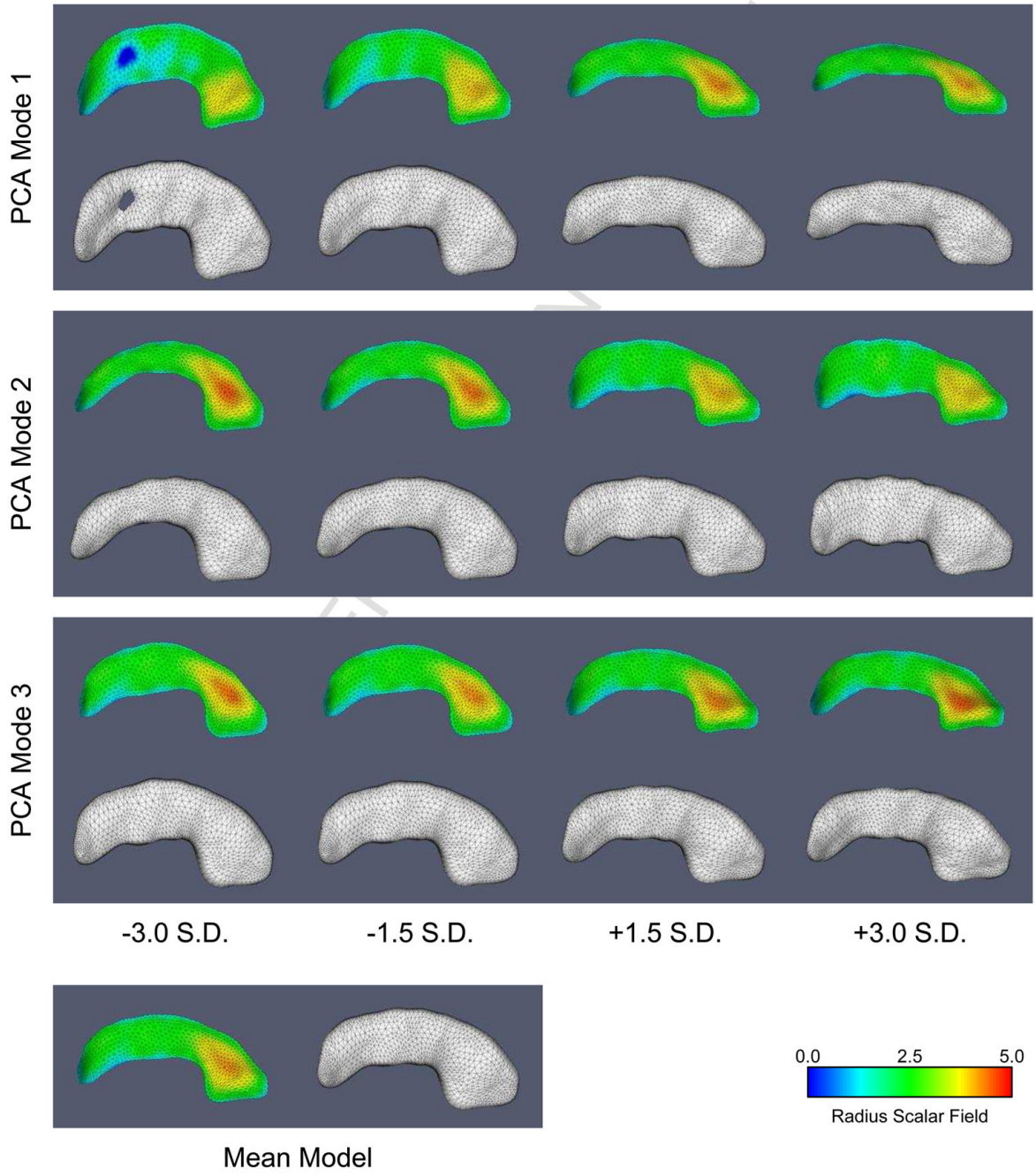


**Fig. 6.**
Principal component analysis in cm-rep parameter space

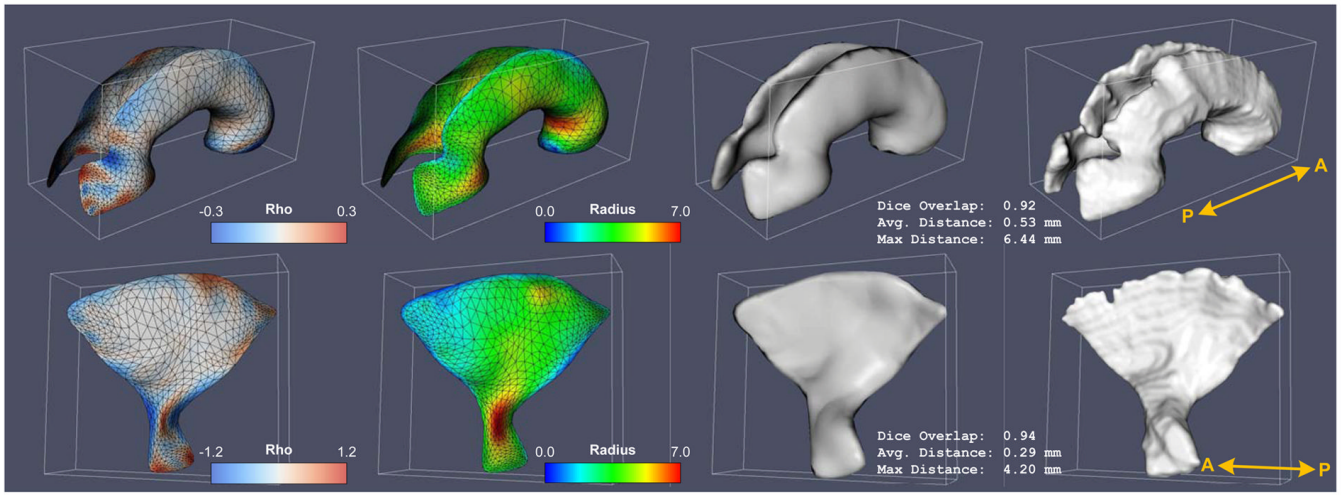


**Fig. 7.**
Examples of cm-rep models fitted to white matter structures extracted from a DTI atlas. This figure illustrates the ability of PDE-based cm-rep models to describe more complex shapes.

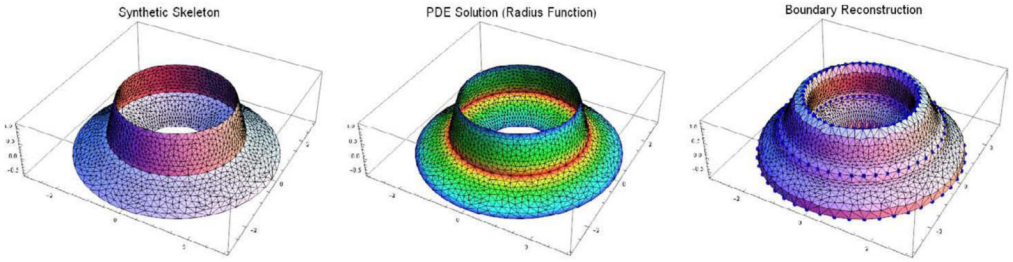


**Fig. 8.**

A toy example of biharmonic PDE-based medal modeling with branching skeletons. The synthetic skeleton (left panel) consists of three branches that join along a circular seam curve. The skeleton has three edge curves, also circles. The inputs to the PDE are $\rho = 0$ on the interior, $\tau = 0.1$ at the edge curves and $\tau = 0.5$ at the seam curves. The radius function $R$ reconstructed by the PDE is plotted in the middle panel, and the reconstructed boundary is given in the right panel. Large blue points indicate the positions on the boundary that correspond to seam and edge curves on the skeleton.

**Table 1**

Accuracy of fitting hippocampus segmentations of deformable cm-rep models. The accuracy obtained using cm-rep models based on the biharmonic equation (BH) is compared to previously published results in (Yushkevich et al., 2006) that used a non-linear Poisson equation (NLP). Each value in the table represents one of five accuracy measures averaged over 89 subjects. The measures include Dice overlap (Dice, 1945) between the interior of the cm-rep model and the segmented hippocampus volume; mean Euclidean distance from the boundary of the cm-rep model to the boundary of the hippocampus; mean distance from the hippocampus to the model; maximum distance (within subject) from the model to the hippocampus; and maximum distance from the hippocampus to the model. The results show a consistent improvement in fitting accuracy with the biharmonic equation approach.

| | Left Hippocampus | | Right Hippocampus | | Both Hippocampi | |
|---|---|---|---|---|---|---|
| | **BH** | **NLP** | **BH** | **NLP** | **BH** | **NLP** |
| Dice Overlap | 0.977 | 0.953 | 0.966 | 0.948 | 0.971 | 0.950 |
| Avg. Dist. Model to Target (mm) | 0.104 | 0.164 | 0.111 | 0.172 | 0.107 | 0.168 |
| Avg. Dist. Target to Model (mm) | 0.121 | 0.187 | 0.133 | 0.200 | 0.127 | 0.194 |
| Max. Dist. Model to Target (mm) | 1.020 | 1.214 | 0.990 | 1.194 | 1.005 | 1.204 |
| Max. Dist. Target to Model (mm) | 1.097 | 1.381 | 1.183 | 1.509 | 1.140 | 1.445 |

**Table 2**

Convergence of quantities derived from a medial model as the resolution of the model is refined. Each row represents a level of subdivision. Levels 1,2 and 3 are compared to level 4, which is the highest-resolution level, in terms of $\varphi$, $R$, $|\nabla \mathbf{m} R|$ and $\mathbf{b}$. For each of these quantities, the mean and maximum difference are averaged over 30 hippocampus models.

| | | | Difference With Finest Model | | | | | | | |
|---|---|---|---|---|---|---|---|---|---|---|
| | | | Phi | | Radius | | \|GradR\| | | Boundary | |
| Level | Vertices | Triangles | *Mean* | *Max* | *Mean* | *Max* | *Mean* | *Max* | *Mean* | *Max* |
| 1 | 853 | 1584 | 0.599 | 2.068 | 0.106 | 0.401 | 0.043 | 0.262 | 0.108 | 0.409 |
| 2 | 3289 | 6336 | 0.267 | 0.891 | 0.048 | 0.194 | 0.021 | 0.150 | 0.046 | 0.195 |
| 3 | 12913 | 25344 | 0.090 | 0.293 | 0.017 | 0.067 | 0.008 | 0.067 | 0.015 | 0.066 |
| 4 | 51169 | 101376 | | | | | | | | |